Check for updates

Received: 20 August 2021 | Revised: 2 December 2021 | Accepted: 2 December 2021

DOI: 10.1002/sia.7055

RESEARCH ARTICLE

SURFACE and INTERFACE ANALYSIS WILEY

Optical constants of organic insulators in the UV range extracted from reflection electron energy loss spectra

Olga Yuryevna Ridzel[1] | Henryk Kalbe[2] | Vytautas Astašauskas[2] | Pavel Kuksa[2] | Alessandra Bellissimo[3] | Wolfgang S. M. Werner[2]

[1]Reservoir potential, Schlumberger Moscow Research Center, Moscow, Russia

[2]Institut für Angewandte Physik, Technische Universität Wien, Vienna, Austria

[3]Institut für Photonik, Technische Universität Wien, Vienna, Austria

Correspondence
Wolfgang S. M. Werner, Institut für Angewandte Physik, Vienna University of Technology, Wiedner Hauptstrasse 8-10, A 1040 Vienna, Austria.
Email: werner@iap.tuwien.ac.at

Funding information
14IND12 EMPIR Project InNanoPart within the European Union's Horizon 2020 Research and Innovation Programme; FP7 People: Marie-Curie Actions Initial Training Network (ITN) SIMDALEE2, Grant/Award Number: PITN 606988; TU Wien Bibliothek

Reflection electron energy loss spectroscopy (REELS) spectra were measured for seven insulating organic compounds (DNA, Irganox 1010, Kapton, polyethylene [PE], poly(methyl methacrylate) [PMMA], polystyrene [PS] and polytetrafluoroethylene [PTFE]). Optical constants and energy band gaps were extracted from the measured REELS spectra after elimination of multiple electron scattering via a deconvolution and fitting the normalised single scattering energy loss spectra to Drude and Drude–Lindhard model dielectric functions, constrained by the Kramers–Kronig sum and *f*-sum rules. Satisfactory agreement is found for those optical constants for which literature data exists. For PTFE, the observed features in the optical data correspond to its electronic structure.

KEYWORDS
electron inelastic mean free path, insulators, optical constants, organic polymers, reflection electron energy loss spectroscopy

1 | INTRODUCTION

Many well-established analytical techniques utilise the interaction of charged particles with matter, for example, electrons, for chemical and structural characterisation of surfaces, such as X-ray photoelectron spectroscopy (XPS),[1] reflection and transmission[2] electron energy loss spectroscopy (REELS and TEELS) and scanning and transmission electron microscopy (SEM and TEM). The evaluation of experimental data acquired with such methods crucially depends on accurate quantitative knowledge of characteristics of electron inelastic scattering or, in other words, electron energy loss process in solids. Such characteristics are the inelastic mean free path (IMFP) and the differential inverse inelastic mean free path (DIIMFP). The DIIMFP describes the distribution of energy losses in an individual inelastic scattering process. The IMFP is the quantity defined as the average distance an electron travels between two successive inelastic collisions measured along the trajectory. This value is of paramount importance in all surface analysis techniques because it determines the surface sensitivity. Furthermore, for ion beam techniques,[3] the dielectric function forms the basis for the calculation of the electronic contribution to the stopping power, the quantity that relates energy losses to the travelled path length. Knowledge of this quantity is essential for low-energy ion scattering, Rutherford backscattering and related techniques to obtain information about the depth of specific scattering centres.

The inelastic interaction of electrons with matter is often described in terms of the dielectric response theory. The dielectric function $\epsilon(\omega,q)$ is a fundamental physical property that describes the response of a material to an external perturbation caused by an electromagnetic wave or a charged particle as a function of the transferred energy ω and momentum q. The dielectric function can be measured by probing a sample surface either with photons[4,5] or electrons[2,6] which implies the measurement of absorptions or energy

This is an open access article under the terms of the Creative Commons Attribution-NonCommercial-NoDerivs License, which permits use and distribution in any medium, provided the original work is properly cited, the use is non-commercial and no modifications or adaptations are made.
© 2022 The Authors. *Surface and Interface Analysis* published by John Wiley & Sons Ltd.

losses, respectively. Both methods have been extensively employed in the past decades. The so-called energy loss function (ELF),

$$\mathrm{ELF} = \mathrm{Im}\left[\frac{-1}{\epsilon(\omega,q)}\right], \quad (1)$$

is usually derived from such measurements. Several main approaches exist for measuring the optical constants of a material: optical reflection,[4,5] absorption and transmission measurements, TEELS[2] and REELS,[7,8] the latter being the simplest technique as far as the experimental effort is concerned.

In the present work, seven organic insulators were investigated using REELS (DNA, Irganox 1010, Kapton, PE, PMMA, PS and PTFE). The experimental data were analysed using the method described in previous studies.[7–9] The normalised DIIMFP was determined by simultaneous deconvolution of a pair of REELS spectra, one of which is measured under more surface-sensitive conditions, while the other is measured under more bulk-sensitive conditions, by an appropriate choice of the energy of impinging electrons and scattering geometry. The DIIMFP is subsequently fitted to a model dielectric function (Drude or Drude–Lindhard) constrained with the Kramers–Kronig sum (KK-sum) and *f*-sum rules. Comparison of our data with those materials for which published optical constants exist (DNA, Kapton, PE, PMMA and PS) generally exhibits good agreement, allowing us to conclude that charging of the insulator surfaces with a beam of low-energy electrons was successfully mitigated. The REELS spectra and the resulting model ELFs of the different organic compounds showed strong similarities, dominated by a feature resembling the $(\pi + \sigma)$-plasmon in graphite, except for PTFE. The features in the dielectric function of PTFE correspond to the (joint) density of states in this material, as reported in the literature.[10–12]

2 | EXPERIMENTAL

The following organic compounds were investigated in this study: (1) Calf thymus DNA (assumed average sum formula $[C_{39}N_{13}O_{24}P_4H_{49}]_n$) thickly deposited by drop-casting from a solution (Sigma-Aldrich, Calf Thymus, Deoxyribonucleic acid D4552) onto a Si wafer, (2) a 48-nm-thick film of the antioxidant Irganox® 1010 (short: Irganox, $C_{73}O_{12}H_{108}$) deposited on a Si/SiO_2 substrate with a 19-nm-thick oxide layer[13] received from NPL, UK, (3) a sample of Kapton® foil ($[C_{22}N_2O_5H_{10}]_n$), (4) a roughly 1.5-mm-thick sample of low-density polyethylene (short: PE, $[C_2H_4]_n$), (5) an approximately 43-nm-thick film of poly(methyl methacrylate) (short: PMMA, $[C_5O_2H_8]_n$) deposited on an Au substrate received from TU Delft, NL, (6) a fragment of a polystyrene cuvette (short: PS, $[C_8H_8]_n$) and (7) a sample of polytetrafluoroethylene foil (short: PTFE, $[C_2F_4]_n$).

The samples of Kapton, PE, PS and PTFE were cleaned by ultrasonication in p.a. grade ethanol immediately prior to introduction into the vacuum. The samples of DNA, Irganox and PMMA were blown clean with helium and otherwise measured as received and were assumed to be in pristine condition.

The REELS spectra were acquired under UHV conditions in a modified VG ESCALAB MkII spectrometer equipped with a hemispherical mirror analyser (HMA) with a sector angle of 150° and operated at a pass energy of 20 eV in constant analyser energy mode. A Kimball Physics ELG-2 electron gun was used as a primary electron source. In order to minimise the effects of radiation damage and sample charging, the primary electron beam was defocussed to a spot size of about 5 mm.

The relative orientations of gun, sample and analyser provide the angles of incidence and emission which need to be taken into account for the extraction of DIIMFPs from the REELS spectra. Values of these parameters for the present measurements are given in Table 1. In the cases of Kapton, PE, PS and PTFE, electron gun, sample surface normal and analyser were arranged in a specular configuration, that is, electron gun, sample and electron analyser were located in the same plane. DNA, Irganox and PMMA were measured with the electron gun oriented at an azimuthal angle ϕ_i of 35° away from the plane of detection. For bulk-sensitive measurements, the electron gun was operated at a primary energy of 1600 eV. The polar angles of incidence θ_i and emission θ_o were both 60° with respect to the surface normal. For surface-sensitive measurements, the primary energy was reduced to 500 eV, and a grazing incidence was achieved by tilting the sample surface normal towards the analyser. The tilting angles used were different for different materials, and the resulting geometry configuration can be found in Table 1.

An important aspect concerning the irradiation of insulators with charged particle beams, such as electrons, is the phenomenon of surface charging. This leads to a change in the surface potential, which may vary with the lateral position.

In general, this has two important consequences for electron scattering experiments: (1) the kinetic energy of the electrons arriving at the surface, the so–called landing energy, will generally differ from the acceleration voltage in the electron source; and (2) the incidence and emission angles may differ from the nominal values governed by the geometrical setup of the experimental system. While these two effects will quantitatively change the interaction, the (positive or negative) acceleration of the incoming particles is compensated during the escape from the surface, implying that the elastic peak and the

TABLE 1 Polar ($\theta_{i,o}$) and azimuthal ($\phi_{i,o}$) angles of incidence and emission (indices *i* and *o*) used for measuring the REELS spectra for bulk- and surface-sensitive conditions at primary energies $E_0 = 1600$ eV and $E_0 = 500$ eV, respectively

	Bulk				Surface			
	$E_0 = 1600$ eV				$E_0 = 500$ eV			
	θ_i	θ_o	ϕ_i	ϕ_o	θ_i	θ_o	ϕ_i	ϕ_o
DNA Irganox PMMA	60°	60°	35°	180°	83°	33°	35°	180°
Kapton PE	60°	60°	0°	180°	87°	33°	0°	180°
PS PTFE	60°	60°	0°	180°	80°	40°	0°	180°

inelastically backscattered electrons in the measured energy spectrum will be located at the expected energy. In the case of the elastic peak, this corresponds to the acceleration voltage in the electron gun. This is in contrast to the spectrum of secondary electrons emitted from the target, which only experience the field due to the surface charge on their way out, and hence, the secondary electron spectrum will shift in energy when the surface is charged. The remaining question of relevance for the interpretation of REELS is how the change in the electron–solid interaction will affect the resulting optical constants.

First of all, it is noted that a change in the landing energy due to surface charging does lead to a different absolute value of the inelastic scattering probability, but the normalised DIIMFP, which is the quantity extracted from the raw data, does not depend appreciably on the actual energy of interaction.[14] The only other parameters used in the present analysis are the so-called partial intensities γ_n, that is, the relative number of electrons experiencing a certain number n of inelastic scatterings, which are needed in the deconvolution of multiple scattering (see Section 3.2). The first-order partial intensity γ_1 is of main importance and always attains values close to unity.[7] The procedure used in the present work is of second order implying that only the first two partial intensities are needed at all, while the result is not much different from a first-order approach. This implies that the only expected influence of charging on the retrieval procedure concerns the first-order partial intensities, which fortunately do not depend critically on the landing energy and the incidence and emission angle, as is shown in Figure 1.

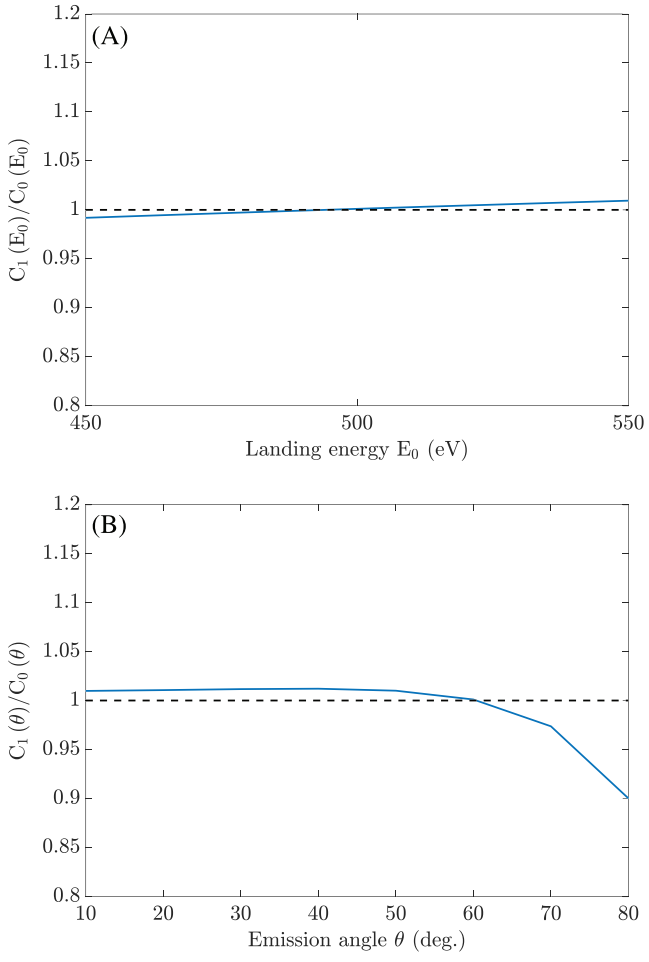

FIGURE 1 The first-order reduced partial intensities of PTFE calculated for (A) different landing energies and for incident and emission angles of $\theta_i = 60°$, $\theta_o = 60°$ and (B) for different emission angles and for $\theta_i = 60°$, and $E_0 = 500$ eV

For some of the measured samples, especially for PTFE and PS, charging effects were indeed observed and manifested themselves as strong fluctuations of the overall signal intensity on a time scale of a few seconds, preventing the recording of usable REELS spectra altogether. This effect was mitigated by defocussing the primary electron beam to a spot diameter of about 5 mm and reducing the beam current to a few nA or less, thereby distributing the incident electron dose over a larger area and hence a longer measurement time (up to 30 min) was required. While residual charging effects cannot be entirely excluded, they are unlikely to have an observable influence, as explained above.

The actual value of the surface potential due to charging was determined for the samples for which the strongest charging effects were observed. This was done by measuring the REELS spectrum with a second analyser in our system, which is a time-of-fight (TOF) analyser. The current used in the TOF experiments was set equal to those in the REELS experiments in order to make a meaningful comparison. For PTFE and PS, the peak of secondary electrons in the TOF spectra was clearly shifted along the time scale, indicating that for the employed conditions (energy, current, scattering geometry), the PS surface becomes negatively charged, while the PTFE surface becomes positively charged. The current used in the TOF experiments was set equal to those in the REELS experiments in order to make a meaningful comparison. This follows from a shift of the onset of the secondary electron peak to smaller flight times (negative surface charging, PS) or larger flight times (positive surface charging, PTFE) due to the fact that the vacuum level is shifted by the surface charge. The extent of surface charging can be estimated from the flight time of the onset of the secondary electron spectrum. The expected value of the flight time of ≈0-eV electrons on a neutral surface was experimentally confirmed on a noncharging surface of highly oriented pyrolytic graphite, with a known work function of HOPG $\varphi = 4.6$ eV by measuring the spectrum with different bias voltages for the TOF spectrometer. For the conditions used to acquire the presented spectra, the absolute value of the surface potential of PS and PTFE was estimated not to exceed ≈5 and ≈20 V, respectively. The above considerations allow us to conclude that the DIIMFP extracted from the present measurements are representative for a neutral surface.

Radiation damage is often a very important issue in electron spectroscopy techniques such as REELS and XPS, especially when organic samples are analysed. Tahir and Tougaard[15] found a significant change in the REELS spectra of PE in consecutive experiments using a focussed electron gun and attributed these to radiation damage. The use of a defocussed electron beam and lower beam currents in this study was also beneficial in reducing radiation damage due to the low flux density of incident electrons in comparison with typical REELS experiments with a focussed beams and relatively short acquisition times. Significant differences between individual scans as demonstrated by Tahir and Tougaard[15] were not observed. XPS measurements were performed before and after the REELS experiments, and no significant changes in

the sample stoichiometries were found. It should be noted that XPS is not sensitive to any changes in the hydrogen content.

3 | DATA ANALYSIS

3.1 | Model dielectric functions and interaction characteristics

The dielectric function $\epsilon(\omega,q)$ is a crucial quantity describing the interaction of charged particles with matter:

$$\epsilon(\omega,q)=\epsilon_1(\omega,q)+i\epsilon_2(\omega,q),$$

where $\epsilon_1(\omega,q)$ and $\epsilon_2(\omega,q)$ are the real (dispersive) and the imaginary (absorptive) part of the dielectric function, respectively. The energy lost by an electron during an inelastic scattering is denoted by ω, and q is the momentum transfer in the collision.

Different approaches are available to model the dielectric function based on a set of bound electrons as oscillators with amplitudes or oscillator strengths A_i, binding energies ω_i and damping parameters Γ_i. One of the simplest and widely used models is the extended Drude model:[16]

$$\begin{aligned}\epsilon_1&=\epsilon_b-\sum_i\frac{A_i\left(\omega^2-\omega_i(q)^2\right)}{\left(\omega^2-\omega_i(q)^2\right)^2+\Gamma_i^2\omega^2},\\ \epsilon_2&=\sum_i\frac{A_i\Gamma_i\omega}{\left(\omega^2-\omega_i(q)^2\right)^2+\Gamma_i^2\omega^2},\end{aligned}\tag{2}$$

with ϵ_b being the background dielectric constant due to the polarizability of the core electrons.[16] Note that in Equation (2) and below, atomic units are used ($\hbar=e=m_e=1$). Another widely used approach is the Drude–Lindhard model that is based on the Drude model with the q-dependence included by Lindhard[17] and consists of expanding the ELF, rather than the dielectric function in a series of oscillators:

$$\mathrm{Im}\left[\frac{-1}{\epsilon(\omega,q)}\right]=\sum_i C_i\frac{\omega\Gamma_i\omega_i(q=0)^2}{\left(\omega^2-\omega_i(q)^2\right)^2+\Gamma_i^2\omega^2},\tag{3a}$$

$$\mathrm{Re}\left[\frac{1}{\epsilon(\omega,q)}\right]=1+\sum_i C_i\frac{\left(\omega^2-\omega_i(q)^2\right)\omega_i(q=0)^2}{\left(\omega^2-\omega_i(q)^2\right)^2+\Gamma_i^2\omega^2},\tag{3b}$$

where C_i is the dimensionless oscillator strength.

Finally, the dispersion of the oscillator resonance energies needs to be taken into account. This is generally done by considering a quadratic dispersion relationship, which in atomic units reads:

$$\omega_i(q)=\omega_i(q=0)+\alpha q^2/2,\tag{4}$$

and making an appropriate choice for the dispersion constant α. It has become customary in Werner et al[7] to use values close to unity for metals and conductors, while for insulators dispersion is usually assumed to be negligible ($\alpha=0$). This approach has also been adopted in the present work.

A test of the consistency of optical data is provided by checking the sum rules. The data in the present work were subjected to the following sum rule checks: the f-sum rule and the KK-sum rule evaluated at $\omega=0$ and $q=0$. The f-sum rule or Thomas–Reiche–Kuhn sum rule is given by[7]

$$f\text{-sum}=\frac{1}{2\pi^2 n_a}\int_0^{\omega_{\max}}\omega\mathrm{Im}\left[\frac{-1}{\epsilon(\omega,q=0)}\right]d\omega,\tag{5}$$

which at $\omega_{\max}\to\infty$ must approach the average atomic number, Z_{av}. The quantity n_a in Equation (5) is the atomic density. In the actual polymer materials different atoms are present. As far as the sum rules are concerned, we assume that each atom is identical and has $n_v=Z_{\mathrm{av}}\cdot n_a$ electrons (therefore, n_v is the valence electron density).

The KK-sum rule is given by[2]

$$1-\mathrm{Re}\left[\frac{1}{\epsilon(\omega=0,q=0)}\right]=\frac{2}{\pi}\int_0^{\omega_{\max}}\frac{1}{\omega}\mathrm{Im}\left[\frac{-1}{\epsilon(\omega,q=0)}\right]d\omega,\tag{6}$$

where $n(\omega=0)$ is the static refractive index. Therefore, the KK-sum can be expressed as follows:

$$\text{KK-sum}=\frac{2}{\pi}\int_0^{\omega_{\max}}\frac{1}{\omega}\mathrm{Im}\left[\frac{-1}{\epsilon(\omega,q=0)}\right]d\omega+\frac{1}{n(\omega=0)^2},\tag{7}$$

which at $\omega_{\max}\to\infty$ must approach 1.

The model dielectric functions introduced above describe free-electron materials but not insulators. Following the customary approach employed by other authors,[15] here and below, we employ the simplest way to model the band gap occurring in the insulator electronic structure by multiplying the ELFs with a step function $\theta(\omega-E_g)$ at the energy loss E_g corresponding to the band gap, where the function $\theta(\omega)$ is the Heaviside step function, and hence zeroing $\mathrm{Im}[-1/\epsilon]$ in the band gap. Because ϵ_1 and ϵ_2, as well as the refractive index n and the extinction coefficient k, are related in a quite fundamental way by means of the Kramers–Kronig dispersion relations, after the zeroing procedure $\mathrm{Re}[1/\epsilon]$ has then to be recovered from $\mathrm{Im}[1/\epsilon]$ via[18,19]

$$\epsilon_1(\omega,q=0)-1=\frac{2}{\pi}\mathrm{P}\int_0^{\omega_{\max}}\frac{\omega'\epsilon_2(\omega',q=0)}{(\omega')^2-\omega^2}d\omega',\tag{8}$$

$$\mathrm{Re}\left[\frac{1}{\epsilon(\omega,q=0)}\right]-1=\frac{2}{\pi}\mathrm{P}\int_0^{\omega_{\max}}\mathrm{Im}\left[\frac{1}{\epsilon(\omega',q=0)}\right]\frac{\omega'd\omega'}{(\omega')^2-\omega^2}.\tag{9}$$

Figure 2 illustrates the difference in the real part of the dielectric function ϵ_1 of DNA (within the Drude model) calculated with and without the Kramers–Kronig transform after zeroing the ELF in the band gap demonstrating insufficient difference between the results of the KK-sum evaluation using Equation (7) with and without doing the Kramers–Kronig transform. Similar results were obtained for all the

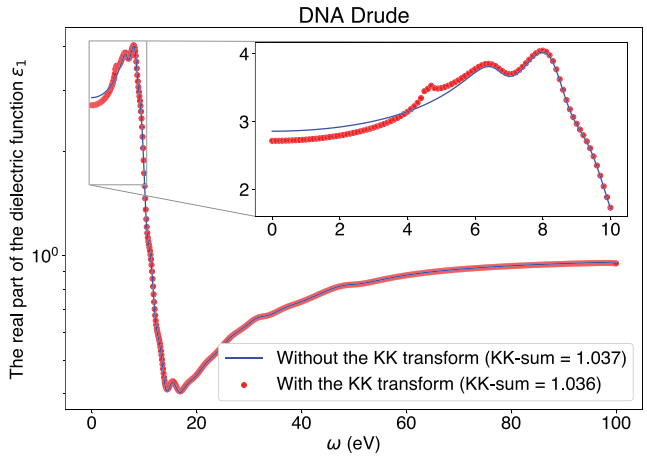

FIGURE 2 The real part of the dielectric function ϵ_1 calculated with and without the Kramers–Kronig transform after the zeroing the ELF in the band gap

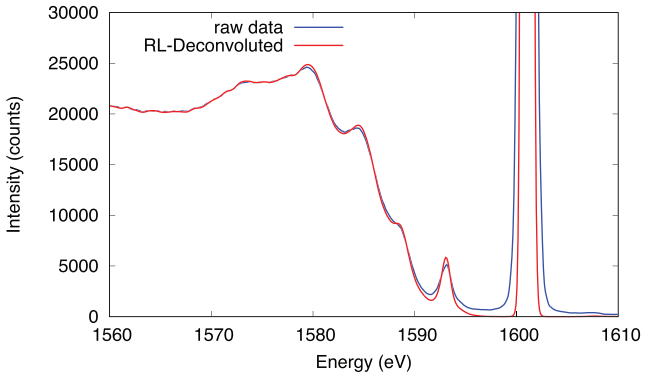

FIGURE 3 Illustration of the Richardson–Lucy deconvolution for the 1600-eV spectrum of PTFE. Blue curve: raw data; red curve: after deconvolution. The full width at half maximum of the elastic peak decreases from 0.43 to 0.34 eV after deconvolution (see text)

materials investigated in this work providing the evidence that the use of the Kramers–Kronig transform is unnecessary in this particular case.

The probability of an electron with a primary energy E_0 to lose energy ω in an individual inelastic scattering event inside the bulk of a solid (subscript *b*) is described by the bulk DIIMFP $W_b(\omega,E_0)$ and is related to the dielectric function $\epsilon(\omega,q)$ as follows:

$$W_b(\omega,E_0)=\frac{1}{\pi E_0}\int_{q_-}^{q_+}\mathrm{Im}\left[\frac{-1}{\epsilon(\omega,q)}\right]\frac{dq}{q}. \tag{10}$$

The limits of integration over the momentum transfer q depend on the incident energy E_0 and the energy loss ω and are a consequence of energy and momentum conservation:

$$q_\pm=\sqrt{2E_0}\pm\sqrt{2(E_0-\omega)}. \tag{11}$$

If dispersion can be neglected ($\alpha=0$), the integral in Equation (10) can be solved analytically as follows:

$$W_b(\omega,E_0)=\frac{1}{\pi E_0}\mathrm{Im}\left[\frac{-1}{\epsilon(\omega,q=0)}\right]\ln\left(\frac{q_+}{q_-}\right). \tag{12}$$

The quantity extracted from the REELS spectra is the *normalised* bulk DIIMFP $w_b(\omega)$:

$$w_b(\omega)=\frac{W_b(\omega,E_0)}{\int_0^{E_0}W_b(\omega,E_0)d\omega}. \tag{13}$$

In the medium electron energy range (100–10,000 eV), this quantity is independent of the energy to a good approximation[14] and is used to retrieve values of the oscillator parameters by finding the set of parameters which minimises the difference between the theoretical and experimental normalised DIIMFP. The proper absolute values of the resulting optical constants are obtained by constraining the parameters during the fit with sum rules, as explained below.

3.2 | Extraction of the normalised DIIMFP from REELS spectra

The present method to obtain the normalised DIIMFP from a pair of experimental REELS described in Werner[8] is based on two main assumptions: (1) The electron reflection process can be described by a Boltzmann-type kinetic equation; and (2) the normalised DIIMFP, that is, the *shape* of the loss distribution, is independent of the energy of interaction. The former requirement is always fulfilled for non-crystalline surfaces, while the latter is true for energies in excess of a few hundred eV.[14] This can be seen from Equation (10) upon realising that the shape of the DIIMFP is only affected by the volume of phase space covered by the limits of momentum transfer $q_\pm$ for any given energy. For energies above a few hundred eV, the effect is negligible.[14]

Each measured REELS spectrum $Y(\omega)$ was first processed by a Richardson–Lucy deconvolution[9] in order to reduce instrumental broadening effects, as shown in Figure 3. Subsequently, the elastic peak was fitted with a Gaussian function and subtracted from the spectrum which is then divided by the elastic-peak intensity and the experimental energy spacing to yield the energy loss spectrum $y(\omega)$ in absolute units of reciprocal eV. The resulting spectrum is the superposition of multiple orders of surface and bulk scattering which need to be deconvoluted to obtain the normalised DIIMFP, that is, the single bulk-scattering energy loss distribution w_b.

Generally, a REELS spectrum contains contributions both from inelastic scattering occurring deep inside the material (described by the DIIMFP, W_b) and a contribution of surface energy losses experienced when an electron crosses the vacuum–solid interface, which is described by the so-called differential surface excitation probability (DSEP), designated by W_s in the following (see previous studies[7,8,14] for a detailed discussion of the meaning of these

quantities). These contributions need to be unravelled to yield the bulk DIIMFP, which is used here to extract the optical constants. This is done by subjecting both spectra of the pair, $y_{1,2}(\omega)$ to the Tougaard–Chorkendorff algorithm[20] in a first step, yielding the intermediate spectra $y^*_{1,2}(\omega)$. The normalised energy loss distribution is then obtained from[8]

$$w(\omega) = u_{10} y_1^*(\omega) + u_{01} y_2^*(\omega) + u_{11} y_1^*(\omega) \otimes y_2^*(\omega), \quad (14)$$

where the symbol $\otimes$ denotes a convolution over the energy and the quantity w represents either the normalised bulk DIIMFP ($w_b(\omega)$) or the DSEP ($w_s(\omega)$) depending on whether the employed coefficients u_{ij} are for bulk and surface scattering as given in Werner.[8] The coefficients u_{ij} are functions of the reduced partial intensities for the spectrum pair, that is, the relative number of electrons experiencing a certain number of volume losses. These quantities depend on the interaction energy and the scattering geometry and were calculated for both spectra of each material using a Monte Carlo (MC) simulation.[21,22] The method described above yields the normalised DIIMFP for bulk scattering, $w_b(\omega)$, in absolute units of reciprocal eV even if the REELS spectra are only measured over a finite energy range.[7,8]

Various alternative approaches have been proposed in the literature to derive the normalised DIIMFP from REELS spectra. Tahir and Tougaard[15] applied the Tougaard–Chorkendorff algorithm[20] to obtain DIIMFPs of some organic samples including PMMA and PE. The 'effective' cross section resulting from the Tougaard–Chorkendorff algorithm meanwhile is in fact known to be not a cross section[8] but rather a weighted superposition of the bulk and surface single scattering loss distribution and a negative mixed term. It is not clear how or whether at all the software of Tahir and Tougaard is taking this into account. Afanas'ev et al[23,24] proposed another approach of deriving the normalised DIIMFP aimed to fit entire REELS spectra instead of using any deconvolution procedure. This method implies that in each fitting step, the normalised DIIMFP and also the normalised DSEP are refined by varying parameters needed for their calculations until the experimental spectrum is reproduced with sufficient accuracy. Such an approach is quite similar to the one used by Vos and Grande[19] and has the advantage of only requiring a single spectrum instead of a pair of spectra. The approach used by Afanas'ev et al. does not allow to obtain optical constants and the ELF whereas this is possible in the case of the method used by Vos and Grande. Owing to the fact that entire spectra are fitted in all the above works, without distinguishing surface and bulk losses, generally makes it more difficult to judge the uniqueness of the obtained solution.

3.3 | Fitting algorithm

The modelled normalised DIIMFP as a function of the oscillator parameters (A_i/C_i, ω_i, Γ_i) is optimised using the nonlinear optimisation library NLopt.[25] The normalised DIIMFP is derived by means of the fitting procedure on the basis of least squares minimisation:

$$\chi^2 = \int_0^{\omega_{max}} \left[w_b(\omega) - w_b^{exp}(\omega) \right]^2 d\omega, \quad (15)$$

by means of the following steps:

1. Set initial oscillator parameters A_i/C_i, ω_i, Γ_i for the model ELF based on the Drude or Drude–Lindhard dielectric function.
2. Calculate the model ELF using the oscillator parameters A_i/C_i, Γ_i, and ω_i (Equations 2 and 3).
3. Calculate the DIIMFP $W_b(\omega, E_0)$ employing Equation (10) and normalise it (Equation 13).
4. Compare the obtained normalised DIIMFP $w_b(\omega)$ with the one extracted from experimental data $w_b^{exp}(\omega)$. Those oscillator parameters that give the minimum value of χ^2 in Equation (15) are considered to be the realistic ones.

Utilising the aforementioned sum rule relations (Equations 5 and 7) allows one to obtain absolute values of the retrieved optical constants. One way of implementing such a scaling procedure is described in Vos and Grande,[19] where at each step of the fitting algorithm, the oscillator parameters are rescaled accordingly depending on the model dielectric function employed. For example, in the case of the Drude model, the amplitudes A_i relate to the density of the valence electrons n_v through the plasmon frequency as $\omega_p^2 = \sum_i A_i = 4\pi n_v$. This relation therefore can be employed as a fit constraint. In the present work, such relations are implemented to the optimisation procedure by invoking nonlinear inequality constraints making sure that the parameters retrieved by the fitting procedure fulfil the *f*-sum rule.

The nonlinear inequality constraints are formulated according to Vos and Grande[19] as follows:

- in the case of the Drude model:

$$\left| \frac{4\pi n_v}{\sum_i A_i} - 1 \right| \approx 0, \quad (16)$$

- in the case of the Drude–Lindhard model:

$$\left| \frac{\sum_i \frac{\pi}{2} C_i \omega_i^2}{2\pi^2 n_v} - 1 \right| \approx 0. \quad (17)$$

In order to obtain meaningful optical constants during the fitting procedure, knowledge of the material-specific valence electron density n_v is required because it serves as a main property to constrain the absolute values of the oscillator amplitudes. However, the value of n_v may be unavailable for some materials whereas in most of cases, the value of the atomic density n_a is known. In the present work, in order to estimate n_v the inner-shell ionisation data from Henke[5] available for energies above 100 eV and up to 30 keV were utilised. First, one must ensure that all inner-shell binding energies for an

investigated material are above 100 eV meaning that below 100 eV, only valence electrons can be excited. If this is the case, then the valence electron density n_v can be evaluated by subtracting from the total electron density $n_e = Zn_a$ the electron density n_{ion} related to the inner shells only which can be obtained via the Bethe sum rule as follows:

$$n_{\text{ion}} = \frac{1}{2\pi^2}\int_{\omega_{\min}}^{\omega_{\max}} \omega \text{Im}\left[\frac{-1}{\epsilon^{\text{Henke}}(\omega, q=0)}\right] d\omega, \tag{18}$$

where $\omega_{\min} = 100$ eV and $\omega_{\max} = 30{,}000$ eV. The valence electron density is then given by

$$n_v = n_e - n_{\text{ion}}. \tag{19}$$

The resulting values of n_v are summarised in Table 3.

4 | RESULTS AND DISCUSSION

Normalised loss spectra obtained as described in the above sections are presented in absolute units of eV^{-1} in Figure 4. Blue curves correspond to more volume-sensitive experimental conditions while red curves are for more surface-sensitive conditions (see Section 2). The panels on the right show the low-loss region where the lowest loss in the bulk DIIMFP (see Figure 5) is highlighted by the green line and corresponds to the HOMO–LUMO distance or band gap energy, E_g.

Two types of differences are seen between the surface- and volume-sensitive loss spectra: (1) At energy losses in the multiple scattering region (energy losses greater or approximately 20 eV), the local minimum in loss spectra at around 30 eV is slightly shallower in the surface-sensitive spectra; and (2) the structure and the intensity of the spectra near the lowest loss indicated by the green line differs for the bulk- and surface-sensitive spectra. The former effect is due to the difference in the effect of multiple scattering on the loss spectra: The loss spectrum is made up of a superposition of multiple self-convolutions of the bulk and surface DIIMFP as well as multiple cross-convolutions between surface and volume single scattering distributions. The peaks in the single scattering loss distributions due to volume (see, e.g., Figure 5) and surface (not shown) scattering are located at about $\hbar\omega_{bulk}$ ~20–25 eV and $\hbar\omega_{surf}$ ~10–15 eV, respectively. Therefore, the contribution to the spectrum of the group of electrons which have experienced one surface and one bulk loss has a (rather broad) peak around ~35 eV. This peak is obviously more pronounced in the surface-sensitive data, leading to a smoother contribution of multiple scattering in the spectra.

The other main difference between the surface and bulk data is the increase in intensity of structures near the lowest loss for the surface-sensitive data. In fact, for some cases, such as PE and PTFE, structures appear in the HOMO–LUMO gap for the surface-sensitive data which are absent or hardly discernible for the bulk-sensitive data. The appearance of such structures are attributed to radiation-induced changes, as was discussed earlier for SiO_2.[27] On the basis of the difference between the surface and bulk data, these changes in the electronic structure are believed to be localised at the very surface. Therefore, the bulk DIIMFP extracted from the pair of spectra is taken to be representative for the bulk material in the following.

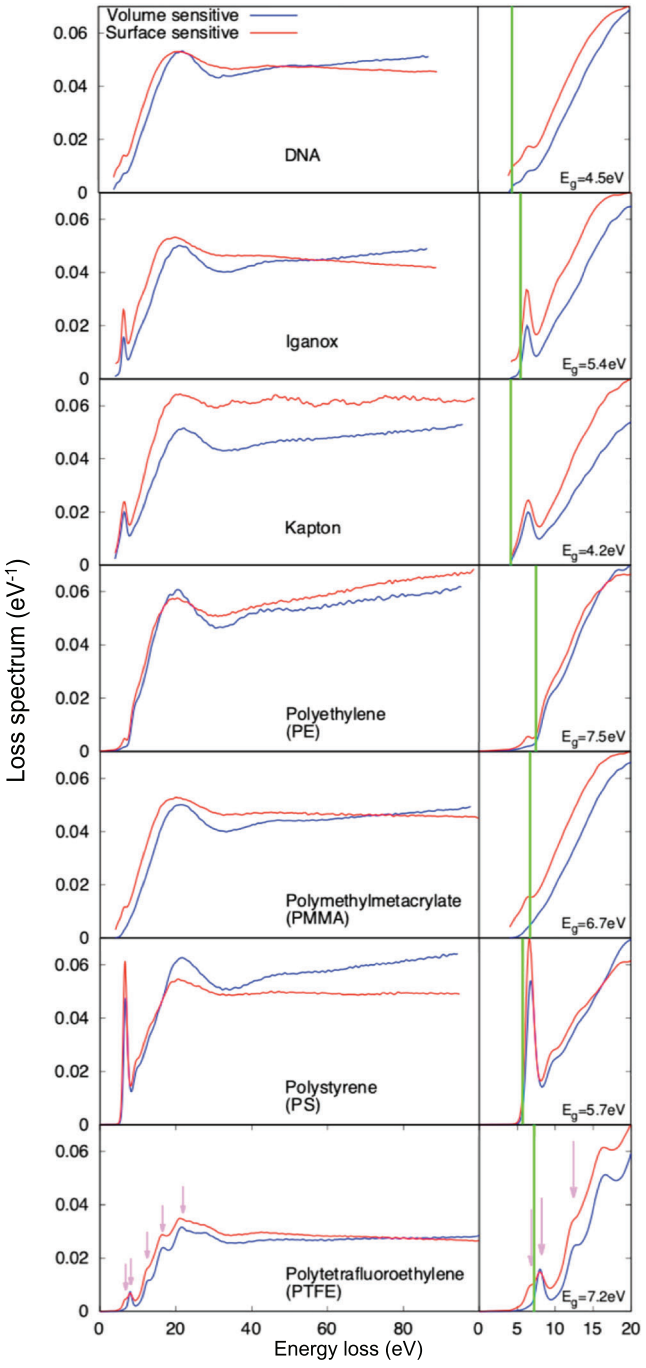

FIGURE 4 Normalised loss spectra of the investigated organic samples in absolute units of eV^{-1}. The measurements using surface-sensitive conditions are given by the red curves, and blue curves correspond to bulk-sensitive conditions. The insets display the low-loss region and the determined lowest loss observed in the bulk DIIMFPs (see text), corresponding to the HOMO–LUMO distance of the studied materials. The numerical values of the band gap energy are given in Table 2. The arrows in the panel for PTFE correspond to the energies of interband transitions observed in Wang et al.[26]

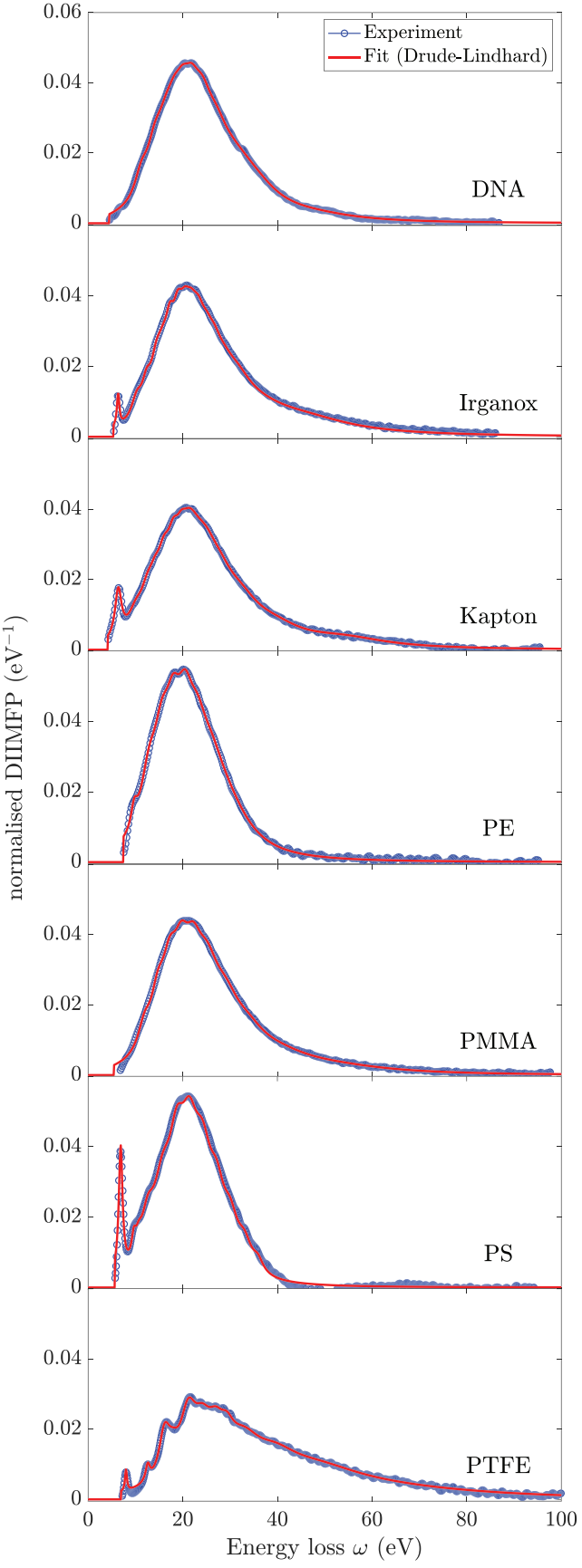

FIGURE 5 Fit of the normalised DIIMFP data extracted from the measured REELS spectra to a Drude–Lindhard model

All spectra share a broad and intense main feature with a maximum at roughly 20 eV, which is attributed to plasmon excitation. The spectra of Irganox, Kapton and PS exhibit sharp features with energy losses between 6 and 7 eV. These represent energy losses due to the excitation of π–π^* transitions, commonly referred to as π-plasmons. This is expected in materials with aromatic rings or more generally for sp^2-hybridised orbitals as in graphite.[28] In the spectra of DNA, PE, PMMA and PTFE, additional features are observed between 4.5 and 8 eV. In the cases of DNA (≈4.5 eV) and PTFE (≈6.5 to 8 eV), these features are also observed in optical absorption spectra[26,29,30] and correspond to near-HOMO–LUMO electronic transitions.

The spectra of most samples are very similar both in shape and intensity. The exception is PTFE which shows additional sharp features overlapping the low-energy shoulder of the plasmon structure. The plasmon loss seems to be significantly broader than in the other compounds. This explains the overall low intensity of the PTFE spectra in the multiple scattering region compared with the other materials. Assuming that the integral inelastic scattering intensity is similar for all materials, a broader single scattering loss distribution automatically implies a lower intensity of the loss spectrum relative to the elastic-peak intensity. Because all data shown in Figure 4 were normalised with the elastic-peak intensity, the low intensity in the energy loss spectrum is therefore consistent with the larger width of the single scattering loss distribution (see also Figure 5).

The structures on the low-loss side of the spectrum of PFTE have been subject of a detailed investigation by Wang et al[26] who compared experimental low-loss and carbon K-shell core-loss spectra with results of density functional theory (DFT) calculations for different conformations of the PTFE polymer. The experimental values of the features observed by these authors (for both the low-loss and core-loss spectra) are in good agreement with electronic interband transitions following from their DFT calculations and are indicated by the arrows in the lower panel of Figure 4. Excellent agreement with the features in the present spectra can be observed. The bulk-sensitive spectrum in Figure 4 corresponds to the so-called H-157 phase consisting of helical chains, containing 15 CF_2 components in seven turns. The surface-sensitive spectrum in our data has an additional peak that according to the calculations in Wang et al[26] corresponds to an interband transition for the disordered helix-reversal defect conformation of PTFE. This supports our interpretation of the features in the surface-sensitive spectra within the HOMO–LUMO gap as being caused by radiation-induced defects and justifies the assignment of the optical data extracted from the normalised bulk DIIMFP as being representative for (defect-free) bulk materials.

The HOMO–LUMO distance was determined on the basis of the volume DIIMFP extracted from the data (see below) by identifying the structure with the lowest energy and fitting a straight line to the region between 10% and 90% of the maximum intensity in the lowest energy feature. The HOMO–LUMO distance, or band gap energy, E_g, was determined from the intersection of the resulting straight line with the energy loss axis. The error in the value of the band gap resulting from this procedure is of the order of 1 eV. The resulting values are compared in Table 2 with data

from the literature. There is a reasonable correlation between the present values and those found in the literature, the latter generally being slightly smaller. This is consistent with the fact that the present results pertain to the bulk electronic structure, as surface energy losses were deconvoluted from the raw data. Radiation induced defects in the near surface region are believed to be eliminated by our deconvolution algorithm employed to separate surface and bulk scattering.

The HOMO–LUMO distance was determined on the basis of the volume DIIMFP extracted from the data by identifying the structure with the lowest energy and fitting. The spectrum pairs shown in Figure 4 measured under bulk- and surface-sensitive conditions were subjected to the deconvolution procedure described in Section 3.2 to yield the normalised DIIMFP. This quantity was fitted to the model dielectric functions using the fitting algorithm described in Section 3.3. The resulting fits are shown in Figure 5. The oscillator parameters for the model dielectric functions are given in Tables A1–A7. Values of the material parameters used in the fitting algorithm and for evaluation of the *f*-sum and the KK-sum rule tests according to Equations (5) and (7) are presented in Table 3.

The experimentally derived DIIMFPs of all materials, shown in Figure 5, are quite similar except for PTFE, the only difference being

TABLE 2 Values of the band gap energy, E_g, or HOMO–LUMO distance determined from the present measurements (left column) compared with values found in the literature (right column)

Material	E_g (eV)	$E_{g,\,lit}$ (eV)
DNA	4.5	4.8[31]
Igranox	5.4	–
Kapton	4.2	2.32[32]
PE	7.5	6.9,[33] 8.8,[34] 7.5,[15] 8.0[35]
PMMA	6.7	4.2,[36] 5.0,[15] 5.0[37]
PS	5.7	4.4[33]
PTFE	7.2	7.7,[38] 6.9–8.2[26]

TABLE 3 Physical quantities used in this study: average atomic number Z_{av}, mass densities ρ, atomic densities n_a, valence electron densities n_v and static refractive indexes $n(0)$ are given for all studied materials

	Z_{av}	ρ (g/cm^3)	n_a (Å^{-3})	n_v (Å^{-3})	$n(0)$
DNA	4.85	1.4[39]	0.09	0.282	1.58[29]
Irganox	3.32	1.077[40]	0.106	0.25	1.535[40]
Kapton	5.0	1.42[41]	0.087	0.29	1.85[42]
PE	2.66	0.94[41]	0.12	0.238	1.52[43]
PMMA	3.6	1.19[41]	0.106	0.267	1.48[44]
PS	3.5	1.06[41]	0.098	0.24	1.58[44]
PTFE	8.0	2.2[41]	0.079	0.387	1.3[45]

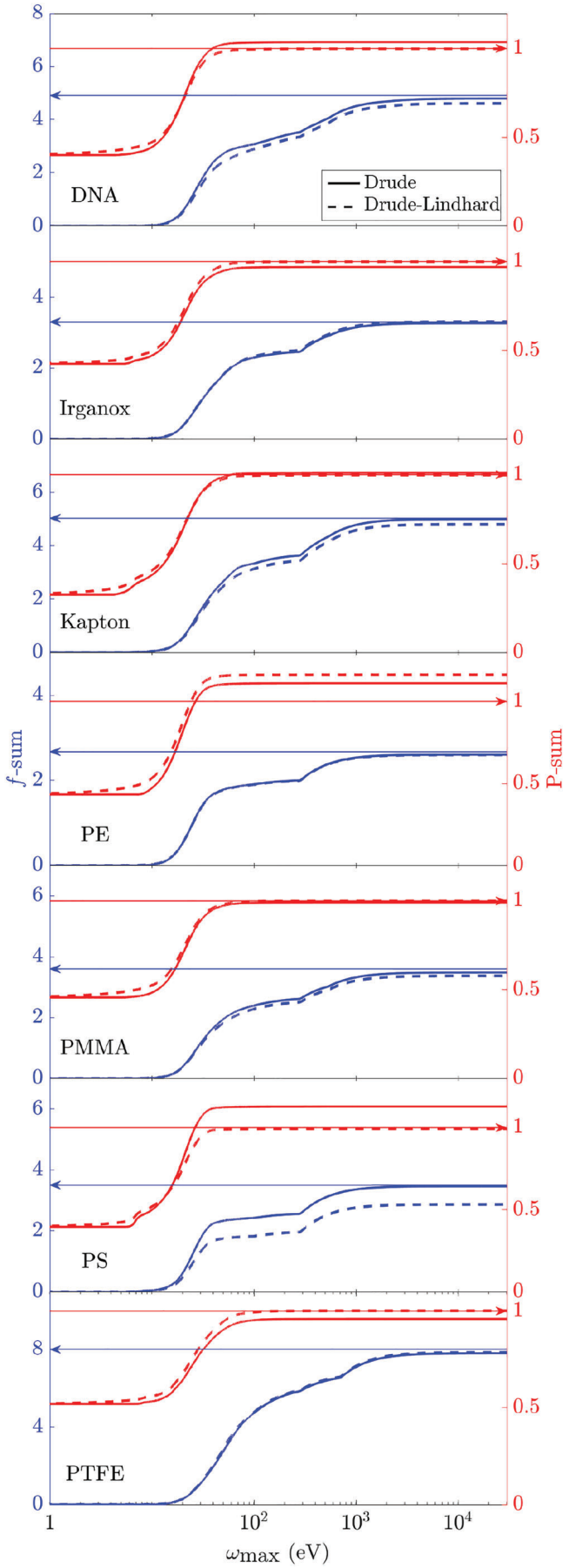

FIGURE 6 The *f*-sum (blue) and KK-sum (red) values as a function of ω_{max}. The solid arrows indicate the limiting theoretical values for the sum rule results

the occurrence and intensity of π-plasmon peaks and the slightly sharper $(\pi+\sigma)$-plasmon in PE and PS. The DIIMFP of PTFE deviates strongly from other materials having a much lower intensity in the energy loss region up to 40 eV and a broader tail beyond that. The Drude–Lindhard model dielectric function (with an artificially introduced band gap) is seen to reasonably fit our experimental data over the entire energy range in the UV regime. The quality of the fit using the Drude parametrisation of optical constants (not shown) is very similar, essentially yielding identical optical constants. The number of oscillators required to obtain a good fit is generally different for the two types of model dielectric functions, as seen in Tables A1–A7. It should be noted that the fit parameters in conjunction with the model dielectric functions provide a means to numerically reproduce our experimentally retrieved ELF, but are generally void of a physical meaning.

The *f*-sum and the KK-sum rules introduced in Equations (5) and (7) were used to constrain the fit of the data to the model ELF. Figure 6 shows the final results of *f*-sum and the KK-sum rule tests as a function of ω_{max}. The maximum *f*-sum values are seen to be slightly below the expected values of the average atomic number Z_{av} for PE and PTFE whereas for other materials, the *f*-sum values are in a good agreement with Z_{av}. The KK-sum values are more than 10% higher than the expected theoretical value of unity for DNA, PE, PS and PTFE, while for others, this value is reasonably reproduced.

Figure 7 shows comparisons between the Drude and Drude–Lindhard ELFs extracted from the normalised DIIMFP fits in the present study (solid curves) and the ELFs found in previous studies[29,37,42,46,47] (black circles) as well as results by Tahir and Tougaard,[15] given by the green curves. Some of these data[15,48] were obtained by a similar technique as in the present work, while the data in previous studies[29,42,46,47] were determined from XUV absorption data and electron energy loss measurements in the transmission electron microscope (TEM-EELS).[37] These literature data obtained from optical techniques and the TEM intrinsically correspond to optical constants for vanishing values of the momentum transfer ($q=0$). The present results were extracted from REELS measurements representing an average over all values of the momentum transfer while assuming that the loss features do not disperse, by choosing the value of the dispersion coefficient $\alpha=0$ in Equation (4) in the fitting procedure. The resulting ELFs shown in Figure 7 agree reasonably well in shape on an absolute scale with optical constants published earlier. The results of Tahir and Tougaard were obtained by using the dispersion coeffficient α as an adjustable parameter, which was found to be small ($\alpha=0.05$). The agreement between the present optical constants and the existing literature data confirms the validity of the selected approach.

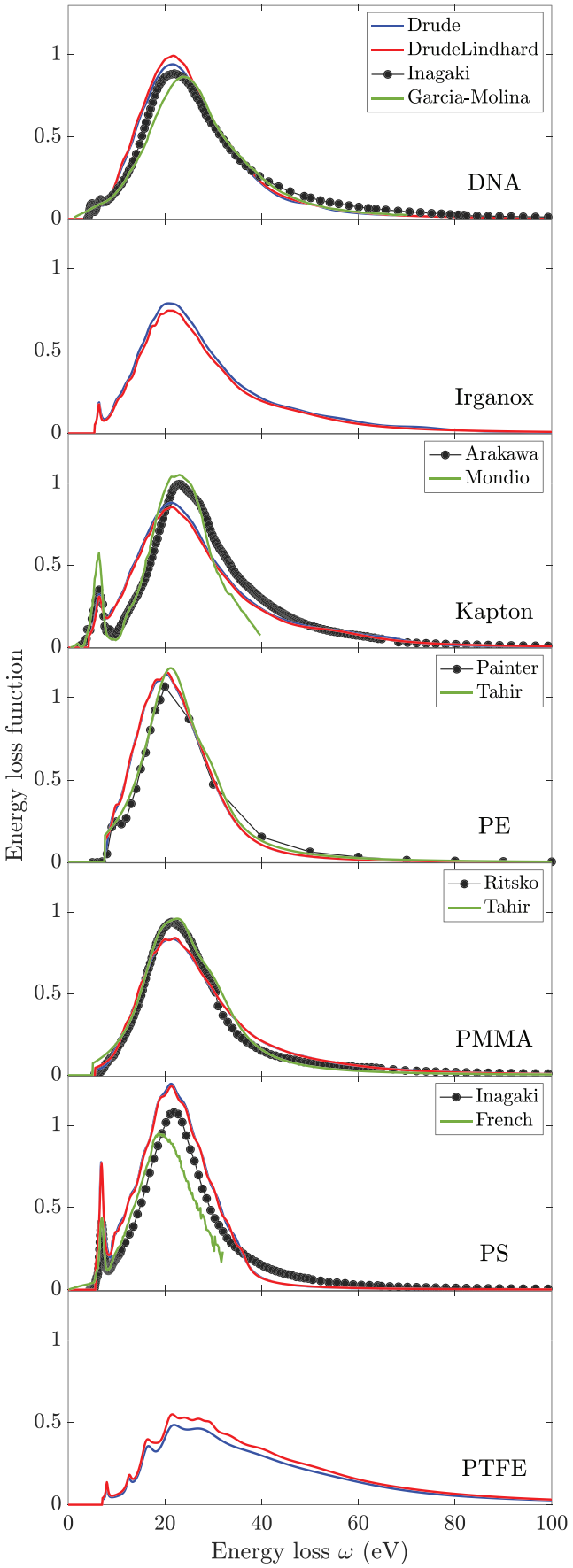

FIGURE 7 Legend on next page.

FIGURE 7 Comparison between the dimensionless energy loss functions (ELFs) extracted from the DIIMFP fits and experimental data found in the literature: DNA from Inagaki et al[29] and Garcia-Molina et al.,[49] Kapton from Arakawa et al[42] and Mondio et al.,[48] PE from Painter et al.,[47] PMMA from Ritsko et al[37] and PS from Inagaki et al[46] and French et al.[50] For PE and PMMA, the ELFs calculated using oscillator parameters from Tahir and Tougaard[15] are also shown

5 | SUMMARY AND CONCLUSIONS

Normalised DIIMFPs for volume inelastic scattering were extracted in absolute units from measured REELS spectra of seven different organic insulators after deconvoluting the surface scattering contributions. The band gap energies obtained from the volume scattering data are in reasonable agreement with data found in the literature, being generally slightly larger. The normalised DIIMFPs were fitted with sets of oscillator parameters using the Drude and Drude–Lindhard model dielectric functions,[19] constrained by the *f*-sum and the KK-sum rules to obtain optical constants on an absolute scale. ELFs calculated on the basis of the present optical constants were compared with various literature sources.[15,29,37,42,46–51] Satisfactory agreement of the optical constants is found with available literature data for DNA, Kapton, PE, PMMA and PS, while for PTFE, a good correspondence of the peaks in the optical constants is found with the bulk electronic structure.

ACKNOWLEDGEMENTS

Financial support by the 14IND12 EMPIR Project InNanoPart within the European Union's Horizon 2020 Research and Innovation Programme and by the FP7 People: Marie-Curie Actions Initial Training Network (ITN) SIMDALEE2 (Grant PITN 606988) is gratefully acknowledged. The computational results presented have been achieved using the Vienna Scientific Cluster (VSC). The authors acknowledge TU Wien Bibliothek for financial support through its Open Access Funding Programme.

DATA AVAILABILITY STATEMENT

Data will be made available upon reasonable request.

ORCID

Olga Yuryevna Ridzel https://orcid.org/0000-0002-9972-3924
Henryk Kalbe https://orcid.org/0000-0002-7162-238X
Vytautas Astašauskas https://orcid.org/0000-0003-0992-8430
Alessandra Bellissimo https://orcid.org/0000-0001-8504-2848
Wolfgang S. M. Werner https://orcid.org/0000-0002-4870-9137

REFERENCES

1. Briggs D, Grant J, eds.. *Surface Analysis by Auger and X-Ray Photoelectron Spectroscopy*: IMPublications; 2003.
2. Egerton R. *Electron Energy-Loss Spectroscopy in the Electron Microscope*: Springer; 2011.
3. Behrisch R, Heiland W, Poschenrieder W, Staib P, Verbeek H. *Ion Surface Interaction, Sputtering and Related Phenomena*: Gordon and Breach Science Publishers; 1973.
4. Palik E. *Handbook of Optical Constants of Solids*. Academic Press; 1998.
5. Henke B, Gullikson E, Davis J. X-Ray Interactions: Photoabsorption, Scattering, Transmission, and Reflection at E = 50-30,000 eV, Z = 1-92. *At Data Nucl Data Tables*. 1993;54(2):181-342. https://doi.org/10.1006/adnd.1993.1013
6. Werner WSM, Schattschneider P. On the energy dissipation process in incoherent electron scattering. *J Electron Spectrosc Relat Phenom*. 2005;143(2–3):65-80. https://doi.org/10.1016/j.elspec.2004.03.011
7. Werner WSM, Glantschnig K, Ambrosch-Draxl C. Optical constants and inelastic electron-scattering data for 17 elemental metals. *J Phys Chem Ref Data*. 2009;38(4):1013-1092. https://doi.org/10.1063/1.3243762
8. Werner WSM. Simple algorithm for quantitative analysis of reflection electron energy loss spectra (REELS). *Surface Science*. 2010;604(3-4):290-299. https://doi.org/10.1016/j.susc.2009.11.019
9. Hummel S, Gross A, Werner WSM. Richardson–Lucy deconvolution of reflection electron energy loss spectra. *Surf Interface Anal*. 2009;41(5):357-360. https://doi.org/10.1002/sia.3006
10. Fahlman M, Clark D, Beamson G, et al. Electronic structure of PTFE substrates to be used for the preparation of ordered organic overlayers. *Synth Met*. 1993;55(1):74-79. https://doi.org/10.1016/0379-6779(93)90912-G
11. Fripiat Joseph G, HFE. The Fourier space restricted Hartree-Fock method for the electronic structure calculation of linear poly(retrafluoroethylene). *Sci China Chem*. 2014;57:1365-1362.
12. Ladik JJ. *Quantum Theory of Polymers as Solids*: Plenum Press; 1995.
13. Shard AG, Havelund R, Spencer SJ, et al. Measuring compositions in organic depth profiling: results from a VAMAS Interlaboratory Study. *J Phys Chem B*. 2015;119(33):10,784-10,797. https://doi.org/10.1021/acs.jpcb.5b05625
14. Werner WSM. Electron transport in solids for quantitative surface analysis. *Surf Interface Anal*. 2001;31:141.
15. Tahir D, Tougaard S. Electronic and optical properties of selected polymers studied by reflection electron energy loss spectroscopy. *J Appl Phys*. 2012;111(5):054101. https://doi.org/10.1063/1.3688327
16. Vos M, Grande PL. How the choice of model dielectric function affects the calculated observables. *Nucl Inst Methods Phys Res Sect B Beam Interact Mater Atoms*. 2017;407:97-109. https://doi.org/10.1016/j.nimb.2017.05.064
17. Lindhard J. On the properties of a gas of charged particles. *Kgl Danske Videnskab Selskab, Mat-fys Medd*. 1954;28:8.
18. Wooten F. Optical properties measurement techniques solar energy materials special issue. *Sol Energy Mater*. 1989;18(3–4):231. https://doi.org/10.1016/0165-1633(89)90057-9
19. Vos M, Grande PL. Extracting the dielectric function from high-energy REELS measurements. *Surf Interface Anal*. 2017;49(9):809-821. https://doi.org/10.1002/sia.6227
20. Tougaard S, Chorkendorff I. Differential inelastic electron scattering cross sections from experimental reflection electron-energy-loss spectra: Application to background removal in electron spectroscopy. *Phys Rev B*. 1987;35(13):6570-6577. https://doi.org/10.1103/PhysRevB.35.6570
21. Werner WSM. Trajectory reversal approach for electron backscattering from solid surfaces. *Phys Rev B*. 2005;71(11):115415. https://doi.org/10.1103/PhysRevB.71.115415
22. Werner WSM. Simulation of electron spectra for surface analysis using the partial-intensity approach (PIA). *Surf Interface Anal*. 2005;37(11):846-860. https://doi.org/10.1002/sia.2103
23. Afanas'ev VP, Gryazev AS, Efremenko DS, Kaplya PS. Differential inverse inelastic mean free path and differential surface excitation probability retrieval from electron energy loss spectra. *Vacuum*. 2017;136:146-155. https://doi.org/10.1016/j.vacuum.2016.10.021
24. Afanas'ev VP, Gryazev AS, Kaplya PS, Ridzel OY. Differential inverse inelastic mean free paths and differential surface excitation probability in aluminium in the energy range of 0.5–120 keV. *J Surf Investig X-*

ray Synchrotron Neutron Tech. 2017;11(4):848-852. https://doi.org/10.1134/S1027451017040164
25. Johnson SG. The NLopt nonlinear-optimization package.
26. Wang C, Duscher G, Paddison SJ. Electron energy loss spectroscopy of polytetrafluoroethylene: experiment and first principles calculations. *Microscopy*. 2014;63:73-83. https://doi.org/10.1093/jmicro/dft046
27. Astašauskas V, Bellissimo A, Kuksa P, Tomastik C, Kalbe H, Werner WSM. Optical and electronic properties of amorphous silicon dioxide by single and double electron spectroscopy. *J Electron Spectrosc Rel Phen*. 2020;241:146829. https://doi.org/10.1016/j.elspec.2019.02.008
28. Werner WSM, Astašauskas V, Ziegler P, Bellissimo A, Linhart L, Libisch F. Secondary electron emission by plasmon induced symmetry breaking in highly oriented pyrolitic graphite (HOPG). *Phys Rev Lett*. 2020;125:196603. https://doi.org/10.1103/PhysRevLett.125.196603
29. Inagaki T, Hamm RN, Arakawa ET, Painter LR. Optical and dielectric properties of DNA in the extreme ultraviolet. *J Chem Phys*. 1974;61(10):4246-4250. https://doi.org/10.1063/1.1681724
30. Seki K, Tanaka H, Ohta T, et al. Electronic structure of poly(tetrafluoroethylene) studied by UPS, VUV absorption, and band calculations. *Phys Scr*. 1990;41(1):167-171. https://doi.org/10.1088/0031-8949/41/1/041
31. Taniguchi M, Kawai T. DNA electronics. *Phys E Low-dimensional Syst Nanostruct*. 2006;33(1):1-12. https://doi.org/10.1016/j.physe.2006.01.005
32. Kleiman J. Protection of materials and structures from space environment. In: ICPMSE Proceedings Series: How Did It All Start? Springer Berlin Heidelberg; 2013; Berlin, Heidelberg:1-11.
33. Ohki Y, Fuse N, Arai T. Band gap energies and localized states in several insulating polymers estimated by optical measurements. In: 2010 Annual Report Conference on Electrical Insulation and Dielectic Phenomena; 2010; West Lafayette, IN, USA:1-4.
34. Lanzillo NA, Breneman CM. Band gap engineering in polymers through chemical doping and applied mechanical strain. *J Phys Condens Matter*. 2016;28(32):325502.
35. Fujihara M, Inokuchi H. Photoemission from polyethylene. *Chem Phys Lett*. 1972;17:554. https://doi.org/10.1016/0009-2614(72)85104-2
36. Sun H, Cao Y, Feng L, Chen Y. Immobilizing photogenerated electrons from graphitic carbon nitride for an improved visible-light photocatalytic activity. *Sci Rep*. 2016;6(1):22808. https://doi.org/10.1038/srep22808
37. Ritsko JJ, Brillson LJ, Bigelow RW, Fabish TJ. Electron energy loss spectroscopy and the optical properties of polymethylmethacrylate from 1 to 300 eV. *J Chem Phys*. 1978;69(9):931-3939. https://doi.org/10.1063/1.437131
38. Palov A, Fujii H, Mankelevich Y, Rakhimova T, Baklanov M. Modelling degradation of PTFE under electron irradiation. *Polym Degrad Stab*. 2012;97(5):802-809. https://doi.org/10.1016/j.polymdegradstab.2012.01.027
39. Jones NC, Hoffmann SV, Mason NJ. Measuring the density of DNA films using ultraviolet-visible interferometry. *Phys Rev E - Stat Nonlinear Soft Matter Physics*. 2013;87(6):060701. https://doi.org/10.1103/PhysRevE.87.060701
40. Irganox 1010. CAS Database. https://www.chembk.com/en/chem/Irganox1010
41. Berger M, Coursey J, Zucker M. Stopping-power and range tables for electrons, protons, and helium ions [Online]. National Institute of Standards and Technology, Gaithersburg, MD. Available: https://dx.doi.org/10.18434/T4NC7P; 2000.
42. Arakawa ET, Williams MW, Ashley JC, Painter LR. The optical properties of Kapton: measurement and applications. *J Appl Phys*. 1981;52(5):3579-3582. https://doi.org/10.1063/1.329140
43. Smith DR, Loewenstein EV. Optical constants of far infrared materials 3: plastics. *Appl Opt*. 1975;14(6):1335. https://doi.org/10.1364/ao.14.001335
44. Zhang X, Qiu J, Li X, Zhao J, Liu L. Complex refractive indices measurements of polymers in visible and near-infrared bands. *Appl Opt*. 2020;59(8):2337. https://doi.org/10.1364/ao.383831
45. Zhang H, Weber SG. *Teflon AF Materials*: Springer Berlin Heidelberg; 2012;307-337.
46. Inagaki T, Arakawa ET, Hamm RN, Williams MW. Optical properties of polystyrene from the near-infrared to the x-ray region and convergence of optical sum rules. *Phys Rev B*. 1977;15(6):3243-3253. https://doi.org/10.1103/PhysRevB.15.3243
47. Painter LR, Arakawa ET, Williams MW, Ashley JC. Optical properties of polyethylene: measurement and applications. *Radiat Res*. 1980;83(1):1. https://doi.org/10.2307/3575254
48. Mondio G, Neri F, Patanè S, Arena A, Marletta G, Iacona F. Optical properties from reflection electron energy loss spectroscopy. *Thin Solid Films*. 1992;207(1-2):313-318. https://doi.org/10.1016/0040-6090(92)90143-Y
49. Garcia-Molina R, Abril I, Kyriakou I, Emfietzoglou D. Inelastic scattering and energy loss of swift electron beams in biologically relevant materials. *Surf Interface Anal*. 2017;49(1):11-17. https://doi.org/10.1002/sia.5947
50. French RH, Winey KI, Yang MK, Qiu W. Optical properties and van der Waals-London dispersion interactions of polystyrene determined by vacuum ultraviolet spectroscopy and spectroscopic ellipsometry. *Aust J Chem*. 2007;60(4):251-263. https://doi.org/10.1071/CH06222
51. Tanuma S, Powell CJ, Penn DR. Calculations of electron inelastic mean free paths. V. Data for 14 organic compounds over the 50-2000 eV range. *Surf Interface Anal*. 1994;21(3):165-176. https://doi.org/10.1002/sia.740210302

How to cite this article: Yuryevna Ridzel O, Kalbe H, Astašauskas V, Kuksa P, Bellissimo A, Werner WSM. Optical constants of organic insulators in the UV range extracted from reflection electron energy loss spectra. *Surf Interface Anal*. 2022;1-14. doi:10.1002/sia.7055

APPENDIX A: VALUES OF THE DRUDE AND DRUDE–LINDHARD OSCILLATOR PARAMETERS FOR THE DIELECTRIC FUNCTION

This appendix contains values of the Drude and Drude–Lindhard oscillator parameters for the dielectric function as given in Tables A1–A7.

TABLE A1 Parameters for the Drude (Equation 2) and Drude–Lindhard (Equation 3) model dielectric functions for DNA resulting from the linear least squares fit of the data for the normalised DIIMFP shown in Figure 5

Drude			Drude–Lindhard		
A_i $(eV)^2$	Γ_i (eV)	ω_i (eV)	C_i	Γ_i (eV)	ω_i (eV)
5.27	1.37	6.78	0.044	3.81	12.96
19.25	1.56	8.56	0.040	4.63	15.25
55.17	2.36	9.89	0.058	4.55	17.03
30.94	2.59	11.66	0.041	4.71	18.92
42.76	3.71	13.50	0.095	5.64	20.94
26.49	4.19	15.99	0.044	4.75	23.33
54.13	7.47	18.73	0.063	14.86	23.87
49.59	9.43	22.99	0.052	5.65	25.99
24.33	8.28	27.96	0.062	10.57	30.36
15.34	6.75	32.70	0.080	16.96	34.01
41.61	85.68	34.97	0.019	70.24	58.82
28.54	12.06	38.11			
9.22	7.76	49.76			

Note: An energy gap was simulated by multiplying the resulting energy loss function with a Heaviside step function located at the the experimentally determined value of the energy gap (see Table 2).

TABLE A2 Same as Table A1 for Irganox

Drude			Drude–Lindhard		
A_i $(eV)^2$	Γ_i (eV)	ω_i (eV)	C_i	Γ_i (eV)	ω_i (eV)
4.83	0.79	6.18	0.014	0.68	6.35
16.22	2.02	9.53	0.028	2.80	10.66
31.49	2.93	11.30	0.026	2.48	12.79
58.09	3.94	13.53	0.035	2.64	14.78
37.06	4.11	16.16	0.030	3.52	16.35
8.87	3.11	18.29	0.043	3.12	17.37
21.31	4.99	19.70	0.057	3.26	19.31
24.68	5.88	21.97	0.043	3.21	21.28
29.09	7.71	25.42	0.076	4.88	23.54
12.74	14.00	30.36	0.062	5.89	26.69
34.89	11.41	30.53	0.036	7.04	30.87
28.98	13.27	37.89	0.059	18.28	35.33
30.77	14.25	46.42	0.040	30.01	42.15
29.04	16.62	56.37	0.026	28.46	50.62
15.27	19.59	72.05			

TABLE A3 Same as Table A1 for Kapton

Drude			Drude–Lindhard		
A_i $(eV)^2$	Γ_i (eV)	ω_i (eV)	C_i	Γ_i (eV)	ω_i (eV)
32.27	1.76	5.49	0.050	1.40	6.41
9.11	1.37	8.62	0.037	5.31	10.54
25.63	2.47	9.91	0.041	3.67	12.60
43.68	3.43	11.63	0.022	2.92	14.33
45.32	5.03	14.05	0.100	4.84	16.88
35.47	6.25	16.63	0.046	3.85	19.43
70.07	9.94	20.07	0.047	4.75	21.60
36.44	9.81	25.30	0.124	8.82	24.09
31.19	11.54	31.20	0.158	12.80	28.26
31.45	15.14	37.52	0.038	12.27	35.96
29.91	16.93	46.15	0.024	34.88	46.33
25.13	12.44	56.03	0.021	23.22	53.12
10.40	7.61	65.02			

TABLE A4 Same as Table A1 for polyethylene (PE)

Drude			Drude–Lindhard		
A_i $(eV)^2$	Γ_i (eV)	ω_i (eV)	C_i	Γ_i (eV)	ω_i (eV)
70.66	1.18	7.92	0.018	1.62	9.79
32.84	2.73	9.51	0.099	4.40	13.07
30.55	2.86	10.77	0.124	4.46	15.79
20.19	3.24	12.41	0.092	3.89	18.09
43.64	12.33	14.35	0.109	4.43	20.57
24.61	4.27	14.80	0.097	5.46	23.22
10.17	3.40	17.22	0.077	7.03	26.31
11.94	3.91	19.55	0.114	12.42	29.92
18.21	6.93	22.46			
31.60	14.43	26.26			
18.33	13.57	26.53			
20.95	16.79	29.75			

TABLE A5 Same as Table A1 for PMMA

Drude			Drude–Lindhard		
A_i $(eV)^2$	Γ_i (eV)	ω_i (eV)	C_i	Γ_i (eV)	ω_i (eV)
11.74	2.08	9.28	0.094	5.86	14.97
25.83	2.14	10.51	0.042	4.09	17.56
21.54	1.97	11.87	0.029	5.07	19.44
26.72	2.53	13.19	0.042	7.18	20.34
27.55	3.13	14.63	0.032	5.08	20.72
29.62	4.06	16.47	0.037	5.48	22.86
27.89	5.14	18.73	0.033	7.13	23.90
23.39	6.19	21.23	0.034	7.14	25.68
39.77	9.50	24.23	0.037	9.02	27.98
29.09	12.02	28.62	0.055	14.11	28.64
28.37	16.36	32.02	0.047	12.63	33.22
22.13	16.91	36.60	0.023	47.23	42.25
16.79	21.99	45.09	0.017	23.75	43.79
20.63	22.37	50.38	0.008	55.84	46.22
40.54	63.83	61.13	0.013	59.81	53.17

TABLE A6 Same as Table A1 for polystyrene (PS)

Drude			Drude–Lindhard		
A_i $(eV)^2$	Γ_i (eV)	ω_i (eV)	C_i	Γ_i (eV)	ω_i (eV)
46.95	0.53	5.70	0.060	0.88	6.91
14.28	1.17	9.07	0.011	1.35	9.76
34.72	3.06	9.87	0.012	2.14	10.86
24.28	4.72	10.52	0.044	3.52	12.77
4.78	2.04	10.71	0.086	4.89	15.76
31.07	3.33	11.89	0.116	4.83	18.99
47.63	4.59	14.27	0.090	4.67	21.51
34.49	5.00	17.06	0.076	4.71	24.12
31.32	6.15	20.33	0.050	4.59	27.11
25.56	6.41	23.87	0.029	4.43	29.98
18.04	5.80	27.57	0.019	4.50	33.39
13.16	5.45	31.41	0.005	4.00	37.00
7.39	4.81	35.34			

TABLE A7 Same as Table A1 for PTFE

Drude			Drude–Lindhard		
A_i $(eV)^2$	Γ_i (eV)	ω_i (eV)	C_i	Γ_i (eV)	ω_i (eV)
1.36	0.46	7.94	0.007	0.56	8.03
7.78	1.21	12.25	0.007	1.16	12.74
61.08	3.37	15.24	0.038	2.76	16.14
35.78	4.48	19.20	0.023	3.50	17.67
17.52	3.43	20.50	0.069	4.30	21.14
110.88	11.79	25.30	0.053	4.94	24.20
110.12	22.23	35.99	0.030	4.35	27.17
303.57	48.94	52.41	0.016	3.82	29.34
			0.060	8.95	32.87
			0.040	11.79	39.17
			0.067	22.97	49.45
			0.072	54.26	57.95